




Optomechanical response of a strongly interacting Fermi gas

Victor Helson ^{1,2} Timo Zwettler ^{1,2} Kevin Roux ^{1,2,3} Hideki Konishi ^{1,2,4} Shun Uchino ⁵ and Jean-Philippe Brantut^{1,2}

¹*Ecole Polytechnique Fédérale de Lausanne, Institute of Physics, CH-1015 Lausanne, Switzerland*

²*Center for Quantum Science and Engineering, Ecole Polytechnique Fédérale de Lausanne, CH-1015 Lausanne, Switzerland*

³*Université Grenoble Alpes, CEA Leti, MINATEC campus, 38054 Grenoble, France*

⁴*Department of Physics, Graduate School of Science, Kyoto University, Kyoto 606-8502, Japan*

⁵*Advanced Science Research Center, Japan Atomic Energy Agency, Tokai 319-1195, Japan*



(Received 4 November 2021; revised 4 May 2022; accepted 7 July 2022; published 12 September 2022)

We study a Fermi gas with strong, tunable interactions dispersively coupled to a high-finesse cavity. Upon probing the system along the cavity axis, we observe a strong optomechanical Kerr nonlinearity originating from the density response of the gas to the intracavity field and measure it as a function of interaction strength. We find that the zero-frequency density response function of the Fermi gas increases by a factor of two from the Bardeen-Cooper-Schrieffer to the Bose-Einstein condensate regime. The results are in quantitative agreement with a theory based on operator-product expansion, expressing the density response in terms of universal functions of the interactions, the contact, and the internal energy of the gas. This provides an example of a driven-dissipative, strongly correlated system with a strong nonlinear response, opening up perspectives for the sensing of weak perturbations or inducing long-range interactions in Fermi gases.

DOI: [10.1103/PhysRevResearch.4.033199](https://doi.org/10.1103/PhysRevResearch.4.033199)

I. INTRODUCTION

Cavity optomechanics allows for the sensing of mechanical displacements with ultimate sensitivity [1–3], by translating the position of an object into the resonance frequency of an optical cavity. This framework naturally describes collective displacements of atoms within a cloud dispersively coupled to light in a high-finesse cavity [4]. The mode of the cavity singles out a particular collective mode of the atomic medium, the amplitude of which directly controls the effective cavity length. The high sensitivity implies that upon injecting light in the cavity, the weak collective displacement induced by the photons feeds back on the cavity resonance position, yielding a Kerr nonlinearity for the cavity or equivalently an effective nonlinearity for the atomic displacement. This hallmark of cavity optomechanics has been observed in the context of cold atoms for tightly confined, thermal clouds [5,6] and homogeneous Bose-Einstein condensates (BECs) [7–9]. Its counterpart for ideal Fermi gases has been predicted [10] but has yet to be observed.

The feedback between the atomic displacement and the intracavity photons is connected by a response function, describing the ability of the gas to adapt its density to an external lattice potential. For weakly interacting bosons, the response is essentially that of a harmonic oscillator, with a frequency directly set by the recoil energy [7] or the

external trap [5]. In contrast, the response of a strongly interacting quantum system depends on the complex interplay between interactions, geometry, and quantum statistics. Although its direct calculation represents a theoretical challenge, it was found in the last decade that many dynamical response functions of the strongly interacting Fermi gas have a universal character captured by Tan's relations [11–14] as observed with a wide variety of spectroscopic probes [15–19].

In this paper, we report on the observation of the optomechanical Kerr nonlinearity of a degenerate, strongly interacting Fermi gas in a high-finesse cavity and measure its dependence on interaction strength in the crossover between the BEC and Bardeen-Cooper-Schrieffer (BCS) regimes [20,21]. In our experiments, the photon wave vector k_c exceeds the Fermi wave vector k_F , so that the response function underlying the nonlinearity has a universal character inherited from the short-range physics of the Fermi gas. We use an operator product expansion (OPE) of the static response function to relate it to two thermodynamic properties of the gas, the contact and the internal energy, and find that it quantitatively describes the scaling of the nonlinearity with interaction strength. This shows that, even though the system is both strongly correlated and driven in the presence of a large feedback, its state remains controlled by a small number of universal parameters, similar to equilibrium properties.

II. OPTOMECHANICAL RESPONSE

The connection between many-body physics in the gas and the optomechanical nonlinearity originates from the structure

Published by the American Physical Society under the terms of the [Creative Commons Attribution 4.0 International](https://creativecommons.org/licenses/by/4.0/) license. Further distribution of this work must maintain attribution to the author(s) and the published article's title, journal citation, and DOI.

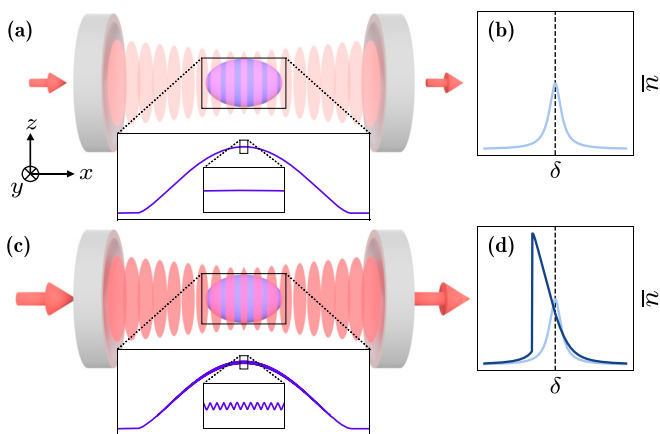


FIG. 1. Concept of the experiment. A weak laser beam dispersively interacts with a Fermi gas held within the mode of a high-finesse cavity. (a) When the probe intensity is low, the dipole force exerted by the intracavity light field is negligible and the atomic density is unperturbed. (b) In that case, the cavity spectrum features a symmetric, Lorentzian shape. (c) For larger probe intensities, the lattice formed by the intracavity light imposes a weak static density modulation on the atoms, modifying the mode overlap with the cavity mode, thus the effective cavity length. (d) The lineshape acquires an asymmetry typical of the Kerr effect. The distinctive sharp edge on the red side of the resonance is due to the onset of bistability.

of the dispersive light-matter coupling Hamiltonian [22,23]

$$\hat{H}_{\text{lm}} = \Omega \hat{a}^\dagger \hat{a} \int d^3r \hat{n}(\mathbf{r}) \cos^2 \mathbf{k}_c \cdot \mathbf{r} = \Omega \hat{a}^\dagger \hat{a} \left(\frac{N}{2} + \hat{M} \right), \quad (1)$$

where Ω is the dispersive coupling strength, \hat{a} annihilates a photon in the cavity with a mode function $\cos \mathbf{k}_c \cdot \mathbf{r}$, \hat{n} is the atomic density operator, and N is the fixed total atom number. We have supposed that the transverse size of the cloud is much smaller than the cavity mode waist. The first part of Eq. (1) represents an average dispersive shift of the cavity while the second describes both a shift of the cavity resonance frequency originating from a collective displacement \hat{M} and an optical lattice with spacing $\pi/|\mathbf{k}_c|$ and depth $\Omega \hat{a}^\dagger \hat{a}$ imprinted onto the atoms.

For an empty cavity or frozen atoms, $\langle \hat{M} \rangle = 0$, so that probing the cavity with vanishingly small probe power yields a symmetric, Lorentzian shaped transmission spectrum with width κ , the inverse photon lifetime, as illustrated in Figs. 1(a) and 1(b). Upon increasing the probe power, the finite intracavity photon number $\bar{n} = \langle \hat{a}^\dagger \hat{a} \rangle$ imprints a density modulation on the atoms, depicted in Fig. 1(c), which yields to first order a displacement

$$\langle \hat{M} \rangle = \frac{N\Omega}{8} \bar{n} \chi^R(2\mathbf{k}_c, 0), \quad (2)$$

where $\chi^R(\mathbf{q}, \omega)$ is the retarded density response function of the gas at frequency ω and wave vector \mathbf{q} [24]. Its imaginary part is connected to the dynamical structure factor via detailed balance and has been measured with high precision [17,25,26]. However the zero-frequency (static) response, which is purely real, has never been measured due to the impossibility to directly observe weak, short-wavelength density perturbations in a strongly interacting system. In the strong

dispersive coupling regime $\Omega N \gg \kappa$, the cavity converts the weak, perturbative displacement into a dispersive shift with a large gain, modifying significantly the transmission of the atom-cavity system, as illustrated in Fig. 1(d).

Accounting for the displacement induced by the probe, described by Eq. (2), as well as the external driving and cavity dissipation in the equations of motion for the intracavity field yields a Kerr optical nonlinearity. Starting from the Hamiltonian (1) and using the input-output formalism in the frame rotating at the drive frequency, the mean-field equations of motion for the intracavity field read

$$\langle \dot{\hat{a}} \rangle = -\left(i\Delta + \frac{\kappa}{2} \right) \langle \hat{a} \rangle - i\Omega \left(\frac{N}{2} + \langle \hat{M} \rangle \right) \langle \hat{a} \rangle - \sqrt{\kappa} b_{\text{in}}, \quad (3)$$

where Δ is the drive-cavity detuning and b_{in} is the driving amplitude. In the steady state, the atomic degrees of freedom are described by Eq. (2), and the intracavity photon number reads (see Appendix A)

$$\bar{n} = \frac{\bar{n}_0}{1 + \frac{4}{\kappa^2} (\delta + \eta \bar{n})^2}, \quad (4)$$

where $\bar{n}_0 = 4|b_{\text{in}}|^2/\kappa$ is the maximum photon number, $\delta = \Delta + \Omega N/2$ is the detuning with respect to the dispersively shifted cavity resonance, and $\eta = \Omega \langle \hat{M} \rangle / \bar{n} = N\Omega^2 \chi^R(2\mathbf{k}_c, 0)/8$ measures the strength of the Kerr nonlinearity. This describes both the intracavity field self-amplified via the atomic medium and the atomic density fluctuations interacting via the cavity field.

III. EXPERIMENT

A. Observation of the optomechanical response

We perform experiments on degenerate balanced two-components Fermi gases of ${}^6\text{Li}$ typically comprising 6×10^5 atoms and held in a crossed dipole trap with frequencies $(\omega_x, \omega_y, \omega_z) = 2\pi \times (187, 565, 594)$ Hz along the x , y , and z directions, respectively. A homogeneous magnetic field \mathbf{B} oriented along the z axis is tuned in the vicinity of a broad Feshbach resonance at 832 G, where the gas explores the BEC-BCS crossover. The gas has a temperature of $T = 0.08(1)T_F$, with $T_F = \hbar(\omega_x \omega_y \omega_z 3N)^{1/3}$ being the Fermi temperature.

The atoms are prepared in the mode of the cavity oriented along x with a finesse of $47'100(700)$ and $\kappa = 2\pi \times 77(1)$ kHz [27]. We probe the system using light linearly polarized along the z axis and matched to the TEM_{00} mode of the cavity. The cavity resonance frequency is detuned by $-2\pi \times 13.9$ GHz from the D1 π transition of ${}^6\text{Li}$ at 832 G, yielding $\Omega = 2\pi \times 11.2$ Hz. With $\Omega N/2\kappa \approx 45$, the system operates deeply in the strong dispersive coupling regime. The probe frequency is dynamically swept from the blue to the red side of the cavity resonance frequency over a range of $2\pi \times 3$ MHz in 3 ms during a single experimental run, and the photon arrival times are recorded with a single photon counting module. The sweep rate was chosen to be slow enough compared with the typical dynamical timescales of the system to ensure that we probe its steady state and fast enough to minimize atomic losses during the probe process. Losses lead to a change of the dispersive coupling during the

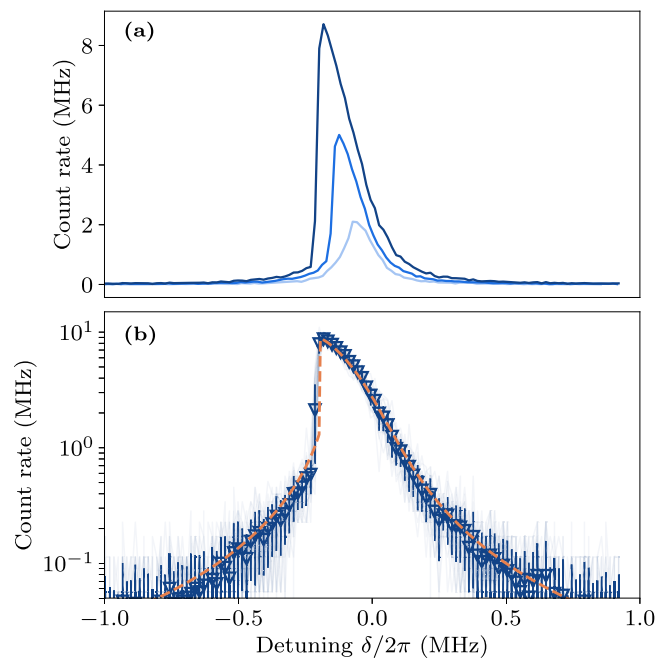


FIG. 2. Optomechanical nonlinearity for the unitary Fermi gas. (a) Transmission spectra of the cavity for increasing probe power (light blue $\bar{n}_0 = 300$, blue $\bar{n}_0 = 700$, and dark blue $\bar{n}_0 = 1300$). For weak probes we observe symmetric Lorentzian profiles (light blue). As the probe power increases, the lineshape is distorted and features a sharp edge on the red side of the resonance (dark blue). $\delta = 0$ is the frequency of the unperturbed, dispersively shifted, atom-cavity resonance. The spectra are averaged 20 times. (b) Aggregated transmission spectra (blue triangles) and individual measurements (gray lines) taken at fixed probe intensity ($\bar{n}_0 = 1300$), in logarithmic scale. Dashed orange line is a fit of Eq. (4) to the averaged curve. The error bars represent the standard deviation over 20 realizations.

sweep representing a systematic error on the nonlinearity (see Appendixes D and F).

Typical transmission lineshapes acquired for a unitary Fermi gas are depicted in Fig. 2(a). For low probe intensity, we record symmetric Lorentzian profiles, with a fitted linewidth of $2\pi \times 116(2)$ kHz, enlarged compared with the inverse photon lifetime by technical fluctuations. As the intracavity photon number is increased, the Kerr nonlinearity originating from atomic displacements distorts the profiles. For the largest probe power, we observe a distinctive sharp edge towards the red side of the cavity resonance, due to the onset of bistability predicted by Eq. [28]. The accurate determination of η , which quantifies the Kerr nonlinearity, requires a high signal-to-noise ratio that we obtain by aggregating multiple traces taken in similar experimental conditions and averaging them (see Appendix E). A fit of Eq. (4) to the averaged profiles then yields a precise value of η . Figure 2(b) displays 20 individual traces, their average and its fitted profile, showing excellent agreement with the model of Eq. (4) over two orders of magnitude of dynamic range.

B. Response in the BEC-BCS crossover

We now observe the variations of the Kerr nonlinearity, and thus of $\chi^R(2\mathbf{k}_c, 0)$ with interaction strength in the BEC-

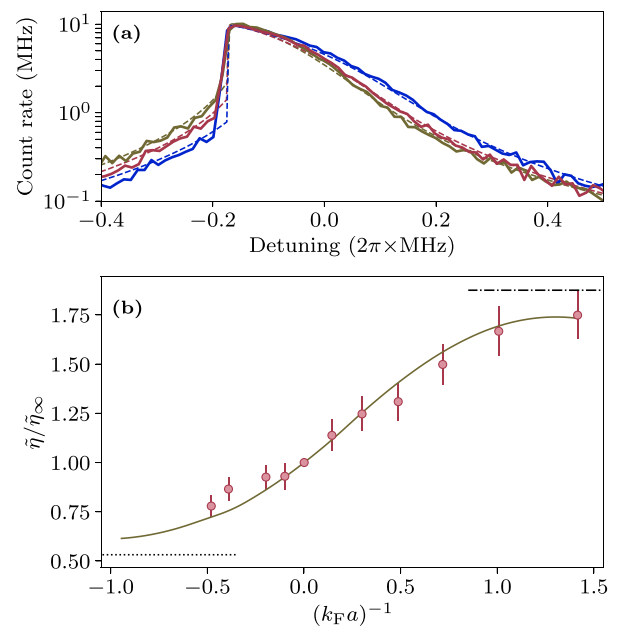


FIG. 3. Optomechanical nonlinearity in the BEC-BCS crossover. (a) Averaged transmission spectra and their fit using Eq. (4) for $1/k_F a = -0.48, 0, 1.42$ (olive, red, and blue, respectively) for fixed atom number and probe power, showing an increase of the nonlinearity with increasing $1/k_F a$. (b) Density response extracted from fits to the distorted transmission profiles, normalized by the value measured at unitarity, as a function of the interaction parameter across the BEC-BCS crossover (red circles). The prediction of Eq. (5) is shown including the internal energy contribution (solid line), based on the contact calculated in Ref. [17]. The horizontal dotted and dash-dotted lines represent values of the density response computed on the BCS side obtained by canceling the contact term of Eq. (5) and on the BEC side by considering the response of a BEC comprising $N/2$ molecules [29], respectively. The error bars represent the uncorrelated combination of statistical fluctuations of the measurement fit uncertainties and systematic effects due to atom losses.

BCS crossover, by repeating this measurement at different magnetic fields around the Feshbach resonance, keeping the other conditions identical. Typical observations are presented in Fig. 3(a) for $B = 710, 832, 950$ G, corresponding to interaction parameters $1/k_F a = -0.48, 0, 1.42$, respectively, with a being the scattering length, together with the fit to Eq. (4) showing a large increase of the response as the gas crosses over from the BCS to the BEC regime.

In our regime, where $2k_c \approx 2.5k_F$, the response function $\chi^R(2\mathbf{k}_c, 0)$ depends on the short-range physics of the gas. This can be exploited to connect the observations of Kerr nonlinearity to the universal thermodynamics of the many-body ground state of the Fermi gas. To this end, we perform an operator product expansion (OPE) of $\chi^R(\mathbf{q}, 0)$ up to second order in k_F/q , leading to the expression [30–32] (see Appendix B)

$$\chi^R(\mathbf{q}, 0) = -\frac{2}{\epsilon_q} - \frac{\pi \tilde{\mathcal{I}}}{\epsilon_q q} \left[1 - \frac{8 + 24\pi - 6\pi^2}{3\pi^2 q a} \right] - \frac{8\tilde{\mathcal{H}}}{3\epsilon_q^2}, \quad (5)$$

where $\epsilon_q = \hbar^2 q^2 / 2m$ and m is the mass of ${}^6\text{Li}$. The expression relates $\chi^R(\mathbf{q}, 0)$ to two universal functions of the interaction

parameter: the total contact $\tilde{\mathcal{I}}$ and total internal energy $\tilde{\mathcal{H}}$ per particle of the cloud. A similar expression at nonzero frequency has been used to relate the dynamical and static structure factors to $\tilde{\mathcal{I}}$ [30–33]. Compared with the structure factor results, the presence of the internal energy contribution is specific to the real part of the response function. Both $\tilde{\mathcal{I}}$ and $\tilde{\mathcal{H}}$ have been computed and measured accurately in the low-temperature regime in the BEC-BCS crossover [15,16,34–39]. The presence of $\tilde{\mathcal{H}}$ in the expansion is necessary in order for the left-hand side of Eq. (5) to match the response of a noninteracting Fermi gas given by Lindhard function in the BCS regime, to second order in k_F/q . On the far BEC side, the OPE suffers from an intrinsic singularity at $qa = 2$ (see Appendix B). There, Eq. (5) should be interpreted as an extrapolation from the large- qa limit to effectively circumvent the singularity in the BEC regime.

To compare with theory, we systematically measure $\tilde{\eta} = \eta/\Omega^2 N$ as a function of B . Here, N is determined independently for each experimental realization before and after the nonlinearity measurement using nondestructive cavity-assisted methods [27]. Converting directly η into an absolute measurement of $\chi^R(2\mathbf{k}_c, 0)$ requires the knowledge of the photon detection efficiency, which is prone to systematic errors. Instead, we normalize the results by the strength of the nonlinearity measured at unitarity $\tilde{\eta}_\infty$, allowing for the precise determination of the relative variations of the response function in the BEC-BCS crossover. This amounts to using the unitary gas data to calibrate the intracavity photon number. The variations are presented in Fig. 3(b), showing a smooth increase by a factor of two from the BCS to the BEC regime.

We calculate $\chi^R(\mathbf{q}, 0)$ from Eq. (5) using the values of $\tilde{\mathcal{I}}$ for harmonically trapped gases in the BEC-BCS crossover calculated by Monte Carlo methods [17] and successfully compared with various experimental observations [17,34,39]. We also infer from it the variations of $\tilde{\mathcal{H}}$ using the adiabatic relation [13] (see Appendix B). The results are shown as a solid line in Fig. 3(b). The agreement with the experimental data is good over the whole range of interaction strength, confirming the deep connection between the optical nonlinearity and the universal, many-body physics of the Fermi gas. This adds the static optomechanical response to the set of response functions experimentally accessible following Tan’s relations. The agreement with Eq. (5) indicates that the increase of nonlinearity towards the BEC regime originates predominantly from the increase of the contact. On the BEC side, the agreement validates our extrapolation of expression (5) and calls for a deeper understanding of the singularities of the OPE.

IV. DISCUSSION AND CONCLUSION

The amplifying ability of the cavity is striking considering that the maximum depth of the probe-induced lattice throughout the entire measurement process is only $0.2E_R$, with $E_R = h \times 73.7$ kHz being the recoil associated with the cavity photons, producing a density modulation with a relative depth of the order of a few percent. The accuracy of our method is mostly limited by atomic losses in the trap, especially on the BEC side, and by probe-induced losses which limit the measurement time and usable probe strength (see Appendix C). While losses are partially of technical origin, we also expect

a fundamental contribution originating from instabilities on the red side of the cavity and amplification due to dynamical backaction on the blue side [40]. Including losses in the microscopic description could be performed in the framework of non-Hermitian perturbation theory [41].

Compared with spectroscopic probes also sensitive to the contact, the optomechanical coupling operates in the static limit where driving the cavity changes the properties of the steady-state of the system. In fact, the correspondence established by Eq. (2) also translates the optical nonlinearity into an interaction between the density fluctuations mediated by light, repulsive on the blue side of the cavity resonance and attractive on the other, similar to cavity-induced squeezing in spin ensembles [42]. Our experiment shows that this effect is controlled by the contact, opening fascinating perspectives for the study of the interplay between contact interactions and long-range correlations.

Last, we could extend our optomechanical response measurement to the vicinity of a photo-association transition, where the dispersive shift acquires directly a contribution proportional to the contact [39]. Correspondingly, the optomechanical response functions such as the contact-density and contact-contact responses, describing three- and four-body effects, which to our knowledge have never been observed experimentally.

ACKNOWLEDGMENTS

We acknowledge discussions with Tobias Donner and Johannes Hofmann and thank Joaquin Drut and Hui Hu for providing the contact data of Ref. [17]. We acknowledge funding from the European Research Council (ERC) under the European Union Horizon 2020 research and innovation programme (Grant Agreement No. 714309), the Swiss National Science Foundation (Grant No. 184654), EPFL, JSPS KAKENHI (Grant No. JP21K03436), the Matsuo Foundation, and the MEXT Leading Initiative for Excellent Young Researchers.

APPENDIX A: PHOTON NUMBER EXPRESSION

We consider the coupling of a Fermi gas to light in an optical cavity in the dispersive limit, where the light-matter coupling is given as Eq. (1) in the main text. In the presence of such a coupling, the Heisenberg-Langevin (input-output) Eq. for the photon field in the frame rotating at a driving frequency, is given by [22,23]

$$\dot{\hat{a}} = -\left(i\Delta + \frac{\kappa}{2}\right)\hat{a} - i\Omega\left(\frac{\hat{N}}{2} + \hat{M}\right)\hat{a} - \sqrt{\kappa}\hat{b}_{\text{in}}, \quad (\text{A1})$$

where Δ is the detuning with respect to the empty cavity, \hat{b}_{in} is the input field, and κ is the cavity decay rate. We then consider the case of the coherent-state input where the coherent-state description for the photon field is reasonable and the corresponding c number field a obeys the following Eq. [22,23]:

$$\dot{a} = -\left(i\Delta + \frac{\kappa}{2}\right)a - i\Omega\left(\frac{N}{2} + \langle\hat{M}\rangle\right)a - \sqrt{\kappa}b_{\text{in}}. \quad (\text{A2})$$

Here we note that the average $\langle \hat{M} \rangle$ contains the light-matter coupling Hamiltonian \hat{H}_{lm} . In the small light-matter coupling limit where the linear-response analysis is allowed, we obtain

$$\langle \hat{M} \rangle \approx \frac{N\Omega}{8} \int_{-\infty}^{\infty} dt' \chi^R(2\mathbf{k}_c, t - t') \bar{n}(t'). \quad (\text{A3})$$

Here we define the retarded density response function per atom,

$$\chi^R(\mathbf{q}, t) = \frac{1}{N} \int d^3R \chi^R(\mathbf{R}, \mathbf{q}, t), \quad (\text{A4})$$

which can be written as the spatial integral of the following local retarded density response function:

$$\begin{aligned} \chi^R(\mathbf{R}, \mathbf{q}, t) &= -i\theta(t) \int d^3r e^{-i\mathbf{q}\cdot\mathbf{r}} \langle [\hat{n}(\mathbf{R} + \mathbf{r}/2), \hat{n}(\mathbf{R} - \mathbf{r}/2)] \rangle_0, \quad (\text{A5}) \end{aligned}$$

with \hat{n} being the density operator of the gas, and $\langle \dots \rangle_0$ denoting the average in the absence of light-matter coupling. To obtain Eq. (A3), we used the local density approximation where the system is locally uniform with translational and inversion symmetries.¹

We now assume the steady-state solution of a where time dependence of the cavity field can be neglected. In this case, $\langle \hat{M} \rangle$ is reduced to

$$\langle \hat{M} \rangle = \frac{N\Omega}{8} \bar{n} \chi^R(2\mathbf{k}_c, 0), \quad (\text{A6})$$

where $\chi^R(2\mathbf{k}_c, 0) = \chi^R(2\mathbf{k}_c, \omega = 0)$. By substituting (A6) into (A2) under $\dot{a} = 0$, we have

$$a = \frac{-2b_{\text{in}}/\sqrt{\kappa}}{1 + \frac{2i}{\kappa}(\delta + \eta\bar{n})}. \quad (\text{A7})$$

By using above the coherent state property $\bar{n} = |a|^2$, Eq. (4) in the main text is obtained.

APPENDIX B: ASYMPTOTIC RETARDED RESPONSE FUNCTION EXPRESSION FROM THE OPERATOR PRODUCT EXPANSION

We discuss the asymptotic form of the density response function in terms of the operator product expansion (OPE). Since the detailed analysis on corresponding time-ordered Green's function has already been done in Refs. [30–32], here we focus on the essential idea and result.

The OPE is a standard approach of quantum field theory which states that the product of local operators at different points in space and time can be expanded in terms of local operators. In the case of the density response function, we can consider the following relation:

$$\hat{n}(\mathbf{R} + \mathbf{r}/2, t) \hat{n}(\mathbf{R} - \mathbf{r}/2, 0) = \sum_m c_m(\mathbf{r}, t) \hat{\mathcal{O}}^m(\mathbf{R}, 0), \quad (\text{B1})$$

where $\hat{\mathcal{O}}^m$ is a local operator and $c_m(\mathbf{r}, t)$ is a function of the relative coordinates. For generic space-time points, the above operator identity may be useless, since the sum in the right-hand side is taken over infinitely many local operators. In the short-range regime that is shorter than mean particle distance ($\approx 1/k_F$) and the inverse of the thermal de Broglie length but is longer than a cutoff length of the effective theory (e.g., van der Waals length in cold gases); however, the OPE becomes a powerful tool in that the first few terms with low scaling dimensions in the operator sum dominate the identity [21].

To proceed with the OPE calculation in terms of quantum field theory, it is convenient to work with the following time-ordered Green's function:

$$\begin{aligned} \chi^T(\mathbf{q}, \omega) &= \frac{-i}{N} \int d^3R \int d^3r \int dt e^{i\omega t - i\mathbf{q}\cdot\mathbf{r}} \\ &\quad \times \langle T[n(\mathbf{R} + \mathbf{r}/2, t)n(\mathbf{R} - \mathbf{r}/2, 0)] \rangle_0, \quad (\text{B2}) \end{aligned}$$

where T denotes time ordering. By using Eq. (B1), the time-ordered function obeys the following relation:

$$\chi^T(\mathbf{q}, \omega) = \sum_m c_m(\mathbf{q}, \omega) \int d^3R \frac{\langle \hat{\mathcal{O}}^m(\mathbf{R}) \rangle_0}{N}. \quad (\text{B3})$$

As defined before, $\langle \dots \rangle_0$ is the average without \hat{H}_{lm} , and therefore $\langle \hat{\mathcal{O}}^m \rangle_0$ is essentially the equilibrium average of a Fermi gas. By using the Feynman diagram technique, we can determine the so-called Wilson coefficient c_m and χ^T . Up to $(k_F/q)^2$, χ^T has been obtained as follows [31,32]:

$$\chi^T(\mathbf{q}, \omega) \approx N c_n(\mathbf{q}, \omega) + c_{\mathcal{I}}(\mathbf{q}, \omega) \tilde{\mathcal{I}} + c_{\mathcal{H}}(\mathbf{q}, \omega) \tilde{\mathcal{H}}. \quad (\text{B4})$$

Here we define

$$c_n(\mathbf{q}, \omega) = \frac{2\epsilon_q}{\omega^2 - \epsilon_q^2}, \quad (\text{B5})$$

$$c_{\mathcal{H}}(\mathbf{q}, \omega) = \frac{4\epsilon_q}{3} \left[\frac{1}{(\omega - \epsilon_q)^3} - \frac{1}{(\omega + \epsilon_q)^3} \right], \quad (\text{B6})$$

$$\begin{aligned} c_{\mathcal{I}}(\mathbf{q}, \omega) &= - \left[A(\mathbf{q}, \omega) \left\{ I_1(\mathbf{q}, \omega) + \frac{2}{A(0)} \frac{1}{\omega - \epsilon_q} \right\}^2 \right. \\ &\quad + A(-\mathbf{q}, -\omega) \left\{ I_1(-\mathbf{q}, -\omega) + \frac{2}{A(0)} \frac{1}{-\omega - \epsilon_{-q}} \right\}^2 \\ &\quad - \frac{[I_2(\mathbf{q}, \omega) + I_3(\mathbf{q}, \omega)]}{2} \\ &\quad - \frac{[I_2(-\mathbf{q}, -\omega) + I_3(-\mathbf{q}, -\omega)]}{2} - \frac{4}{A(0)} \frac{1}{\omega^2 - \epsilon_q^2} \\ &\quad - \frac{2}{A(0)} \left\{ \frac{1}{(\omega - \epsilon_q)^2} + \frac{1}{(\omega + \epsilon_q)^2} \right\} \\ &\quad \left. - \frac{4\epsilon_q}{3A(0)} \left\{ \frac{1}{(\omega - \epsilon_q)^3} - \frac{1}{(\omega + \epsilon_q)^3} \right\} \right], \quad (\text{B7}) \end{aligned}$$

with $\epsilon_q = q^2/(2m)$, $A(0) = -\frac{4\pi a}{m}$,

$$A(\mathbf{q}, \omega) = \frac{\frac{4\pi}{m}}{-\frac{1}{a} + \sqrt{-m[\omega - q^2/(4m)] - i0^+}}, \quad (\text{B8})$$

$$I_1(\mathbf{q}, \omega) = \int \frac{d^3k}{(2\pi)^3} \frac{1}{\epsilon_{\mathbf{k}} \omega - \epsilon_{\mathbf{k}} - \epsilon_{\mathbf{k}+\mathbf{q}} + i0^+}, \quad (\text{B9})$$

¹To be precise, the local translational symmetry ensures that the local density response function is expressed with the Fourier component of the relative coordinate (A5), and the local inversion symmetry ensures $\chi^R(\mathbf{R}, -2\mathbf{k}_c, t) = \chi^R(\mathbf{R}, 2\mathbf{k}_c, t)$.

$$I_2(\mathbf{q}, \omega) = \int \frac{d^3k}{(2\pi)^3} \frac{1}{\epsilon_{\mathbf{k}}^2} \left[\frac{1}{\omega - \epsilon_{\mathbf{k}} - \epsilon_{\mathbf{k}+\mathbf{q}} + i0^+} - \frac{1}{\omega - \epsilon_{\mathbf{q}} + i0^+} \right], \quad (\text{B10})$$

$$I_3(\mathbf{q}, \omega) = \int \frac{d^3k}{(2\pi)^3} \frac{1}{\epsilon_{\mathbf{k}}\epsilon_{\mathbf{k}+\mathbf{q}}} \frac{1}{\omega - \epsilon_{\mathbf{k}} - \epsilon_{\mathbf{k}+\mathbf{q}} + i0^+}. \quad (\text{B11})$$

We now apply the above result for the retarded density response function. To this end, we focus on the spectral representation of Green's function [24], which allows us to relate χ^T to χ^R . By using this, it is straightforward to show

$$\text{Re}[\chi^R(\mathbf{q}, \omega)] = \text{Re}[\chi^T(\mathbf{q}, \omega)], \quad (\text{B12})$$

$$\chi^R(\mathbf{q}, 0) = \text{Re}[\chi^R(\mathbf{q}, 0)]. \quad (\text{B13})$$

Thus, it turns out that $\chi^R(\mathbf{q}, 0)$ can directly be determined from Eq. (B4). To obtain a simpler expression, we finally perform integrals in I_1 , I_2 , and I_3 . First, by using

$$\frac{1}{AB} = \int_0^1 dx \frac{1}{[Ax + B(1-x)]^2}, \quad (\text{B14})$$

$$\int \frac{d^3k}{(2\pi)^2} \frac{1}{[k^2 + \alpha^2 - i0^+]^2} = \frac{1}{8\pi\alpha}, \quad (\text{B15})$$

we can show

$$I_1(\pm\mathbf{q}, 0) = -\frac{m^2}{4q}. \quad (\text{B16})$$

In addition,

$$I_2(\pm\mathbf{q}, 0) = -\frac{2m^3}{\pi q^3}, \quad (\text{B17})$$

can be shown by using

$$\frac{1}{AB^2} = 2 \int_0^1 \frac{1-x}{[Ax + (1-x)B]^3}, \quad (\text{B18})$$

$$\int \frac{d^3k}{(2\pi)^2} \frac{1}{[k^2 + \alpha^2 - i0^+]^3} = \frac{1}{32\pi\alpha^3}. \quad (\text{B19})$$

Finally, by using

$$\frac{1}{ABC} = 2 \int_0^1 dx \int_0^{1-x} dy \frac{1}{[Ax + By + C(1-x-y)]^3}, \quad (\text{B20})$$

$$\int_0^1 dx \int_0^{1-x} dy \frac{1}{\{1 - (x-y)^2\}^{3/2}} = 1, \quad (\text{B21})$$

we obtain

$$I_3(\pm\mathbf{q}, 0) = -\frac{2m^3}{\pi q^3}, \quad (\text{B22})$$

and we also obtain

$$A(\pm\mathbf{q}, 0) = \frac{8\pi}{mq(1 - \frac{2}{qa})}, \quad (\text{B23})$$

such that the OPE expansion for $\chi^R(\mathbf{q}, 0)$ reads

$$\chi^R(\mathbf{q}, 0) = -\frac{2N}{\epsilon_q} - \frac{8\tilde{\mathcal{H}}}{3\epsilon_q^2} - \frac{\pi\tilde{\mathcal{I}}}{2\epsilon_q q} \left[\frac{1}{1 - \frac{2}{qa}} - \frac{8}{\pi qa(1 - \frac{2}{qa})} + \frac{16}{\pi^2 (qa)^2 (1 - \frac{2}{qa})} - \frac{8}{3\pi^2 qa} \right]. \quad (\text{B24})$$

This expression diverges for $qa = 2$, such that in the BEC regime it becomes uncontrolled. However, close to the unitary regime $qa \gg 1$, the expression above reduces to Eq. (4) in the main text

$$\chi^R(\mathbf{q}, 0) = -\frac{2N}{\epsilon_q} - \frac{8\tilde{\mathcal{H}}}{3\epsilon_q^2} - \frac{\pi\tilde{\mathcal{I}}}{2\epsilon_q q} \left[1 - \frac{8 + 24\pi - 6\pi^2}{3\pi^2 qa} \right]. \quad (\text{B25})$$

which is regular in the BEC regime. The OPE results with and without the large- qa limits are presented in Fig. 4.

APPENDIX C: EXPERIMENTAL PROCEDURE

We prepare a quantum degenerate, strongly interacting Fermi gas of ${}^6\text{Li}$ following the method described in Ref. [27]. At the end of the all-optical preparation, we perform transmission spectroscopy while holding the Fermi gas in a crossed optical dipole trap with trapping frequencies of $2\pi \times (187, 565, 594)$ Hz along the longitudinal and transversal directions of the cavity.

The spectroscopic measurement consists of four probe pulses with π polarization, during which we sweep the frequency of the probe beam across the cavity resonance. First,

we perform a pulse with fast sweep rate to determine the resonance of the dispersively shifted cavity, allowing us to infer the atom number in a nondestructive way [27]. This is followed by a second pulse to measure the optomechanical response of the Fermi gas as described in the main text. The third and fourth pulses measure the dispersively shifted cavity resonance after the response measurement to infer losses and the cavity resonance without atoms, respectively.

The probe power is optimized for the highest signal-to-noise ratio and is limited by the dynamic range of the single-photon counter. At high photon flux the detector response becomes nonlinear, which introduces a bias in the Kerr effect determination. By recording the position of the cavity resonance without atoms, we can correct for slow drifts in the experimental lock chain and exactly determine the dispersive shifts.

APPENDIX D: ATOM-NUMBER DETERMINATION AND LOSSES

The atom number is extracted from the dispersive shift of the cavity resonance with respect to the bare cavity $\delta_{\text{at}} = \frac{N\Omega}{2}$ with light shift $\Omega = \frac{g_0}{\Delta_a}$, atom number N , single photon-atom

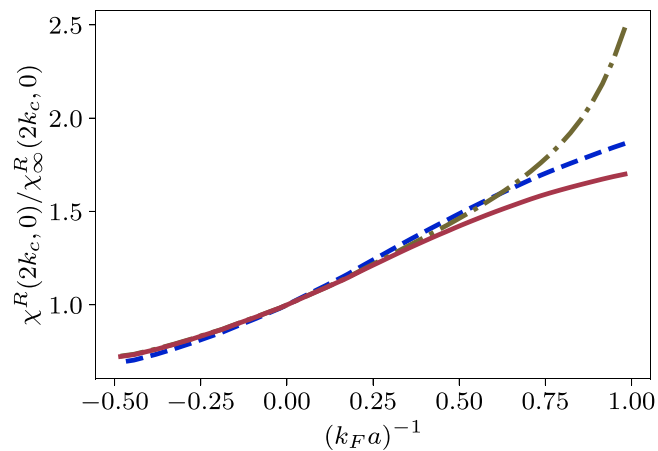


FIG. 4. Comparison of different OPE expressions for $\chi^R(\mathbf{q}, 0)$ as a function of $(k_F a)^{-1}$ for a trap-averaged system of 6×10^5 atoms and other parameters as in the main text. The OPE expressions show all very similar behavior in the unitary regime. However, in the BEC regime the expression without $qa \gg 1$ approximation (B24) shows a divergence approaching $qa = 2$ (olive dash dotted line), whereas the OPE expression with $qa \gg 1$ approximation (B25) (red solid line) circumvents the singular behavior and should be interpreted as an extrapolation from the large- qa limit. For comparison, (B25) without the internal energy contribution is also shown (blue dashed line).

coupling strength g_0 , and atom-cavity detuning Δ_a . We take $D1\pi$ and $D2\pi$ transitions into account to infer the total atom number:

$$N = \frac{2\delta_{\text{at}}}{g_{D1\pi}^2/\Delta_{D1\pi} + g_{D2\pi}^2/\Delta_{D2\pi}}, \quad (\text{D1})$$

with the coupling strengths $g_{D1\pi} = 2\pi \times 276$ kHz, $g_{D2\pi} = 2\pi \times 391$ kHz and the detunings of the cavity resonance from the respective atomic transitions at 832 G of $\Delta_{D1\pi} = -2\pi \times 13.9$ GHz and $\Delta_{D2\pi} = -2\pi \times 23.6$ GHz.

Using a fast and nondestructive measurement of the dispersive shift, we determine the atom number before and after the optomechanical response measurement and infer the atomic losses encountered during the measurement. We investigated the response and losses as a function of the measurement duration, as shown in Fig. 5 for the unitary Fermi gas. For durations shorter than 5 ms, the losses are below 2%, while reaching up to 7.2% for a sweep duration of 30 ms.

Losses originate both from the finite lifetime of the gas in the trap and from the measurement itself. To disambiguate between these two effects, we measure the losses due to the finite lifetime of the gas, depending on interaction strength, by replacing the slow optomechanical response measurement between the two dispersive shift measurements by another dispersive shift measurement. This also allows us to infer the exact atom number at the position of the slow sweep. The results for the losses corresponding to an optomechanical response measurement duration of 3 ms are presented in Fig. 6, which shows a strong increase of the loss rate towards the BEC side due to three-body losses [20]. We find that the total losses at 832 G are below 2%, matching the value measured for Fig. 5(b). Therefore, for durations of 3 ms, trap losses have a small contribution for a unitary gas, and we infer

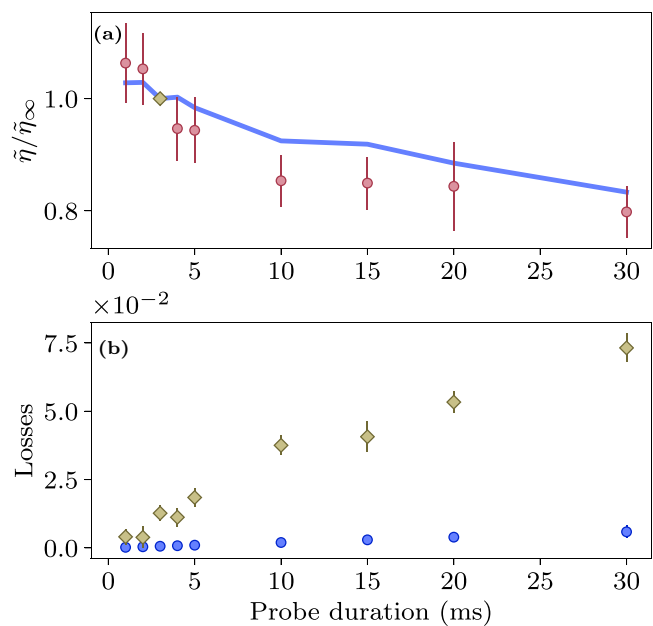


FIG. 5. (a) Static response per atom $\tilde{\eta}$ as a function of the probe duration over a frequency range of $2\pi \times 2.7$ MHz for a unitary Fermi gas, all other parameters identical to the main text. $\tilde{\eta}$ is normalized to the response per atom $\tilde{\eta}_\infty$ at 3 ms probe duration used in the experiment at 832 G (olive diamonds). Simulation of the effect of losses on the fitted static response (light blue line). (b) Total atomic losses as a function of the sweep duration inferred from two dispersive shift measurements respectively performed before and after the slow sweep (olive diamonds). The chosen probe duration of 3 ms minimizes measurement-induced losses to below 1.4%, which would systematically shift down the static response of the gas for longer sweep durations. The effect of probe-induced losses becomes more significant for longer probe durations, whereas the trap losses remain small over the time of probing (blue circles).

measurement-induced losses of 1.3%. On the BEC side, we also infer measurement-induced losses below 2% for 3 ms duration, hence the choice for the main text data presented in Fig. 5(a). This ensures that the measurement-induced losses do not shift the cavity resonance by more than its linewidth while maintaining a high signal-to-noise ratio of the photon count rate at all detunings.

Note that the equilibrium condition for the atomic gas is easily fulfilled since we increase the probe power from the background to its maximal value in about 1 ms, which is long compared with the dynamical timescale of atomic motion given by the recoil time of $13.57 \mu\text{s}$.

Even though losses are small compared with the total atom number, the change of dispersive shift during the measurement yields a systematic decrease of the observed nonlinearity, which we account for in the error bars (see below).

APPENDIX E: DATA ANALYSIS

The photon count rate \bar{n}_{det} recorded from transmission spectroscopy is related to the intracavity photon number \bar{n} by

$$\bar{n}_{\text{det}} = \epsilon \frac{\kappa}{2} \bar{n}, \quad (\text{E1})$$

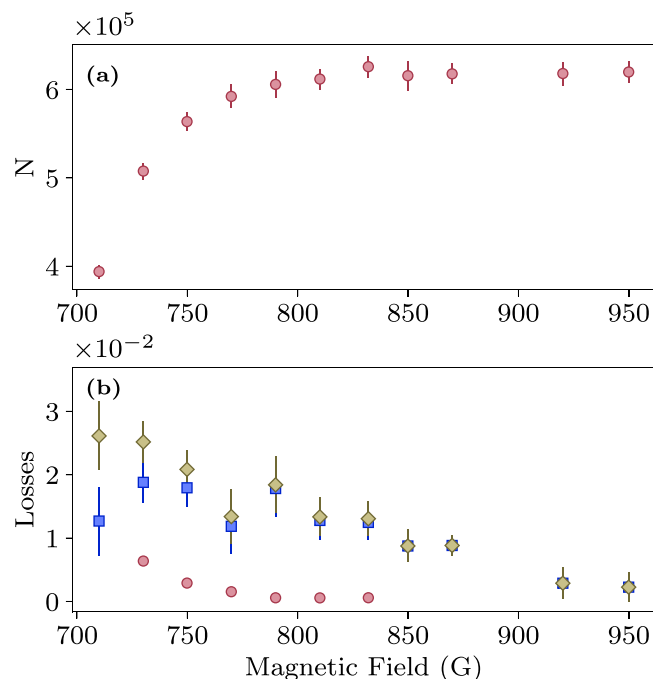


FIG. 6. (a) Total atom number measured before the nonlinearity measurement as a function of magnetic field. (b) Total losses during the nonlinearity measurement as a function of magnetic field (olive diamonds) compared with trap losses due to the finite atomic lifetime (red circles) and probe induced losses (blue squares).

with photon-detection efficiency ϵ and cavity intensity decay rate κ . Inserting Eq. (E1) into Eq. (A7) yields the model for the Kerr nonlinear resonator:

$$\bar{n}_{\text{det}} = \frac{\bar{n}_0^{\text{det}}}{1 + \left(2\frac{\delta}{\kappa} + 4\frac{\eta'}{\kappa^2}\bar{n}_{\text{det}}\right)^2} \quad (\text{E2})$$

with the maximal detected photon count rate $\bar{n}_0^{\text{det}} = \epsilon\frac{\kappa}{2}\bar{n}_0$ and Kerr nonlinearity $\eta' = \eta/\epsilon$. Eq. (E2) reduces to a third-order polynomial in \bar{n}_{det} , which can be solved for each value of δ . Figure 7 displays the two stable solutions of

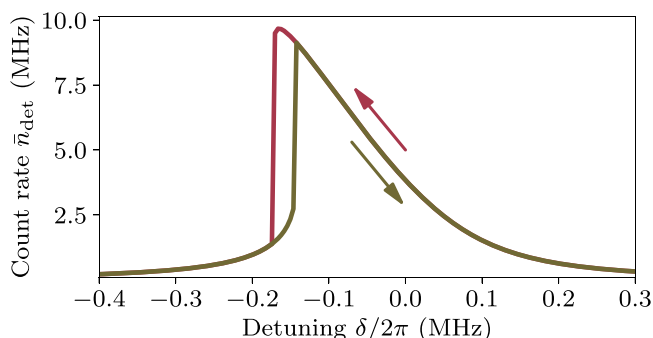


FIG. 7. Solution of the cubic polynomial given by Eq. (E2) for the fitted parameters at 832 G. The two stable solutions of the cubic polynomial, which are explored by sweeping the frequency from the blue to the red side (red) and from the red to the blue side (olive). A sweep direction downward in frequency is chosen in the experiment to avoid measurement-induced heating resulting from a sudden increase in intracavity photon number.

the Eq. for a set of parameters reproducing the experimental conditions. In the bistable regime the Eq. has three real solutions, of which the two shown solutions correspond to the stable branches of the model. We pick the largest of the two real stable solutions which corresponds to our procedure of downwards sweeping the probe frequency. That branch is depicted by the red curve of Fig. 7. The downward sweep direction is chosen to avoid measurement-induced heating due to a sudden increase in intracavity photon number.

The numerical solution is then used as a fit function for \bar{n}_{det} as a function of δ . We acquire 30 transmission spectra obtained with the same experimental parameters on different realizations of the atomic samples. We overlap the spectra on their sharp edge before averaging them together and fitting the averaged profile on Eq. (E2) to extract η , as depicted by Fig. 2(b) of the main text. We found that the fitted value of the nonlinearity parameter η is sensitive to the shape of the tails of the transmission profile. To obtain a good agreement between the fit and the averaged profiles, we fit the logarithm of the latter, thus equally weighting data points at the peak and in the wings of the profile. This results in the typical data shown in Fig. 2(b) of the main text, and their fit with good agreement over two orders of magnitude. In the procedure, we fix \bar{n}_0^{det} to the maximal detected number of photons. Moreover, the effective cavity linewidth is increased compared with the fast sweep configuration due to technical fluctuations at the slow sweep rate at which the experiment is operated. Measuring the linewidth of the cavity with slow sweep rates, we obtain $\kappa = 2\pi \times 116(2)$ kHz, which we also set as fixed in the fitting procedures.

The statistical errors are estimated by using a bootstrap method. We randomly resample the 30 profiles taken for one set of experimental conditions to produce 20 datasets, which are then averaged and fit, yielding 20 statistical realizations of η for the initial 30 spectra. These realizations are averaged, their mean used as the measured value of η in the main text, and their standard deviations used as statistical error estimate. These are combined with estimates for the systematic error due to atom losses (see below) to produce the error bars.

APPENDIX F: SYSTEMATIC ERROR DUE TO LOSSES

In Fig. 5(a), we display the effect of losses on the fitted static response. By assuming a constant atom loss rate L over the probe duration for the trap and probe-induced losses as observed in Fig. 5(b), we simulate the distortion of the Kerr nonlinear profile by modifying Eq. (E2) to

$$\eta'(t) = \tilde{\eta}'\Omega^2(N - Lt), \quad (\text{F1})$$

$$\delta(t) = \frac{d\Delta}{dt}t + \Omega/2(N - Lt), \quad (\text{F2})$$

with the detuning from the bare cavity resonance Δ . We then fit the simulated, distorted profiles using Eq. (E2) and use the result to estimate the effect of losses on the static response [light blue line Fig. 5(a)]. As expected, we observe that losses decrease the fitted static response, due to the variations of the

dispersive shift during the measurement. The result of the loss simulation reproduces well the tendency of the fitted static response, as can be seen in Fig. 5(a). For the chosen probe duration of 3 ms, we perform the simulation for the losses at each magnetic field. Using this simulation, we estimate the

systematic error of the fitted η' to be 4% compared with its undistorted value. This is now included in the error bar for the data shown in the main text through independent error combination with the statistical fluctuations inferred from the bootstrap method (see above).

-
- [1] A. A. Clerk, M. H. Devoret, S. M. Girvin, F. Marquardt, and R. J. Schoelkopf, Introduction to quantum noise, measurement, and amplification, *Rev. Mod. Phys.* **82**, 1155 (2010).
- [2] M. Aspelmeyer, T. J. Kippenberg, and F. Marquardt, Cavity optomechanics, *Rev. Mod. Phys.* **86**, 1391 (2014).
- [3] H. Yu, L. McCuller, M. Tse, N. Kijbunchoo, L. Barsotti, and N. Mavalvala, Quantum correlations between light and the kilogram-mass mirrors of LIGO, *Nature (London)* **583**, 43 (2020).
- [4] D. M. Stamper-Kurn, in *Cavity Optomechanics: Nano- and Micromechanical Resonators Interacting with Light*, edited by M. Aspelmeyer, T. J. Kippenberg, and F. Marquardt Quantum Science and Technology (Springer, Berlin, Heidelberg, 2014), pp. 283–325.
- [5] S. Gupta, K. L. Moore, K. W. Murch, and D. M. Stamper-Kurn, Cavity Nonlinear Optics at Low Photon Numbers from Collective Atomic Motion, *Phys. Rev. Lett.* **99**, 213601 (2007).
- [6] T. P. Purdy, D. W. C. Brooks, T. Botter, N. Brahms, Z.-Y. Ma, and D. M. Stamper-Kurn, Tunable Cavity Optomechanics with Ultracold Atoms, *Phys. Rev. Lett.* **105**, 133602 (2010).
- [7] F. Brennecke, S. Ritter, T. Donner, and T. Esslinger, Cavity optomechanics with a Bose-Einstein condensate, *Science* **322**, 235 (2008).
- [8] S. Ritter, F. Brennecke, K. Baumann, T. Donner, C. Guerlin, and T. Esslinger, Dynamical coupling between a Bose-Einstein condensate and a cavity optical lattice, *Appl. Phys. B: Lasers Opt.* **95**, 213 (2009).
- [9] H. Kessler, J. Klinder, M. Wolke, and A. Hemmerich, Optomechanical atom-cavity interaction in the sub-recoil regime, *New J. Phys.* **16**, 053008 (2014).
- [10] R. Kanamoto and P. Meystre, Optomechanics of a Quantum-Degenerate Fermi Gas, *Phys. Rev. Lett.* **104**, 063601 (2010).
- [11] S. Tan, Energetics of a strongly correlated Fermi gas, *Ann. Phys. (NY)* **323**, 2952 (2008).
- [12] S. Tan, Generalized virial theorem and pressure relation for a strongly correlated Fermi gas, *Ann. Phys. (NY)* **323**, 2987 (2008).
- [13] S. Tan, Large momentum part of a strongly correlated Fermi gas, *Ann. Phys. (NY)* **323**, 2971 (2008).
- [14] E. Braaten, D. Kang, and L. Platter, Universal relations for a strongly interacting Fermi gas near a Feshbach resonance, *Phys. Rev. A* **78**, 053606 (2008).
- [15] N. Navon, S. Nascimbène, F. Chevy, and C. Salomon, The equation of state of a low-temperature Fermi gas with tunable interactions, *Science* **328**, 729 (2010).
- [16] J. T. Stewart, J. P. Gaebler, T. E. Drake, and D. S. Jin, Verification of Universal Relations in a Strongly Interacting Fermi Gas, *Phys. Rev. Lett.* **104**, 235301 (2010).
- [17] S. Hoinka, M. Lingham, K. Fenech, H. Hu, C. J. Vale, J. E. Drut, and S. Gandolfi, Precise Determination of the Structure Factor and Contact in a Unitary Fermi Gas, *Phys. Rev. Lett.* **110**, 055305 (2013).
- [18] C. Shkedrov, Y. Florshaim, G. Ness, A. Gandman, and Y. Sagi, High-Sensitivity rf Spectroscopy of a Strongly Interacting Fermi Gas, *Phys. Rev. Lett.* **121**, 093402 (2018).
- [19] B. Mukherjee, P. B. Patel, Z. Yan, R. J. Fletcher, J. Struck, and M. W. Zwierlein, Spectral Response and Contact of the Unitary Fermi Gas, *Phys. Rev. Lett.* **122**, 203402 (2019).
- [20] W. Ketterle and M. W. Zwierlein, Making, probing and understanding ultracold Fermi gases, *Riv. Nuovo Cimento* **31**, 247 (2008).
- [21] *The BCS-BEC Crossover and the Unitary Fermi Gas*, Lecture Notes in Physics, edited by W. Zwerger (Springer, Berlin, Heidelberg, 2012).
- [22] H. Ritsch, P. Domokos, F. Brennecke, and T. Esslinger, Cold atoms in cavity-generated dynamical optical potentials, *Rev. Mod. Phys.* **85**, 553 (2013).
- [23] F. Mivehvar, F. Piazza, T. Donner, and H. Ritsch, Cavity QED with quantum gases: new paradigms in many-body physics, *Adv. Phys.* **70**, 1 (2021).
- [24] A. L. Fetter and J. D. Walecka, *Quantum Theory of Many-Particle Systems* (Dover Publications, Inc., Mineola, 2003).
- [25] C. Carcy, S. Hoinka, M. G. Lingham, P. Dyke, C. C. N. Kuhn, H. Hu, and C. J. Vale, Contact and Sum Rules in a Near-Uniform Fermi Gas at Unitarity, *Phys. Rev. Lett.* **122**, 203401 (2019).
- [26] H. Biss, L. Sobirey, N. Luick, M. Bohlen, J. J. Kinnunen, G. M. Bruun, T. Lompe, and H. Moritz, Excitation Spectrum and Superfluid Gap of an Ultracold Fermi Gas, *Phys. Rev. Lett.* **128**, 100401 (2022).
- [27] K. Roux, V. Helsen, H. Konishi, and J. P. Brantut, Cavity-assisted preparation and detection of a unitary Fermi gas, *New J. Phys.* **23**, 043029 (2021).
- [28] S. L. McCall, Instabilities in continuous-wave light propagation in absorbing media, *Phys. Rev. A* **9**, 1515 (1974).
- [29] L. Pitaevskii and S. Stringari, *Bose-Einstein Condensation and Superfluidity*, International Series of Monographs on Physics (Oxford Academic, Oxford, 2016).
- [30] D. T. Son and E. G. Thompson, Short-distance and short-time structure of a unitary Fermi gas, *Phys. Rev. A* **81**, 063634 (2010).
- [31] W. D. Goldberger and I. Z. Rothstein, Structure-function sum rules for systems with large scattering lengths, *Phys. Rev. A* **85**, 013613 (2012).
- [32] J. Hofmann, Current response, structure factor and hydrodynamic quantities of a two- and three-dimensional Fermi gas from the operator-product expansion, *Phys. Rev. A* **84**, 043603 (2011).
- [33] J. Hofmann and W. Zwerger, Deep Inelastic Scattering on Ultracold Gases, *Phys. Rev. X* **7**, 011022 (2017).

- [34] E. D. Kuhnle, S. Hoinka, H. Hu, P. Dyke, P. Hannaford, and C. J. Vale, Studies of the universal contact in a strongly interacting Fermi gas using Bragg spectroscopy, *New J. Phys.* **13**, 055010 (2011).
- [35] E. D. Kuhnle, H. Hu, X.-J. Liu, P. Dyke, M. Mark, P. D. Drummond, P. Hannaford, and C. J. Vale, Universal Behavior of Pair Correlations in a Strongly Interacting Fermi Gas, *Phys. Rev. Lett.* **105**, 070402 (2010).
- [36] Y. Sagi, T. E. Drake, R. Paudel, R. Chapurin, and D. S. Jin, Breakdown of the Fermi Liquid Description for Strongly Interacting Fermions, *Phys. Rev. Lett.* **114**, 075301 (2015).
- [37] G. Ness, C. Shkedrov, Y. Florshaim, O. K. Diessel, J. von Milczewski, R. Schmidt, and Y. Sagi, Observation of a Smooth Polaron-Molecule Transition in a Degenerate Fermi Gas, *Phys. Rev. X* **10**, 041019 (2020).
- [38] M. Horikoshi, M. Koashi, H. Tajima, Y. Ohashi, and M. Kuwata-Gonokami, Ground-State Thermodynamic Quantities of Homogeneous Spin-1/2 Fermions from the BCS Region to the Unitarity Limit, *Phys. Rev. X* **7**, 041004 (2017).
- [39] H. Konishi, K. Roux, V. Helsen, and J.-P. Brantut, Universal pair polaritons in a strongly interacting Fermi gas, *Nature (London)* **596**, 509 (2021).
- [40] T. J. Kippenberg and K. J. Vahala, Cavity opto-mechanics, *Opt. Express* **15**, 17172 (2007).
- [41] L. Pan, X. Chen, Y. Chen, and H. Zhai, Non-Hermitian linear response theory, *Nat. Phys.* **16**, 767 (2020).
- [42] I. D. Leroux, M. H. Schleier-Smith, and V. Vuletić, Implementation of Cavity Squeezing of a Collective Atomic Spin, *Phys. Rev. Lett.* **104**, 073602 (2010).